






Bioinformatic Mining and Structure-Activity Profiling of Baeyer-Villiger Monooxygenases from *Mycobacterium tuberculosis*

Nicolas Tomas,^a Dimitri Leonelli,^a Martin Campoy,^a Sylvain Marthey,^b Nguyen-Hung Le,^{a*} David Rengel,^a Véronique Martin,^b Adrian Pál,^c Jana Korduláková,^c Nathalie Eynard,^d Valérie Guillet,^a Lionel Mourey,^a Mamadou Daffé,^a  Anne Lemassu,^a  Gwenaëlle André,^b  Hedia Marrakchi^a

^aInstitut de Pharmacologie et de Biologie Structurale, IPBS, Université de Toulouse, CNRS, UPS, Toulouse, France

^bMalAGE, INRAE, AgroParisTech, Université Paris-Saclay, Jouy-en-Josas, France

^cDepartment of Biochemistry, Faculty of Natural Sciences, Comenius University in Bratislava, Bratislava, Slovakia

^dLMGM-CBI, UMR 5100, Université de Toulouse, CNRS, UPS, Toulouse, France

Nicolas Tomas and Dimitri Leonelli contributed equally to this work. Author order was determined on the basis of seniority.

ABSTRACT *Mycobacterium tuberculosis* is the etiological agent of tuberculosis (TB), one of the deadliest infectious diseases. The alarming health context coupled with the emergence of resistant *M. tuberculosis* strains highlights the urgent need to expand the range of anti-TB antibiotics. A subset of anti-TB drugs in use are prodrugs that require bioactivation by a class of *M. tuberculosis* enzymes called Baeyer-Villiger monooxygenases (BVMOs), which remain understudied. To examine the prevalence and the molecular function of BVMOs in mycobacteria, we applied a comprehensive bioinformatic analysis that identified six BVMOs in *M. tuberculosis*, including Rv3083 (MymA), Rv3854c (EthA), Rv0565c, and Rv0892, which were selected for further characterization. Homology modeling and substrate docking analysis, performed on this subset, suggested that Rv0892 is closer to the cyclohexanone BVMO, while Rv0565c and EthA are structurally and functionally similar to MymA, which is by far the most prominent type I BVMO enzyme. Thanks to an unprecedented purification and assay optimization, biochemical studies confirmed that all four BVMOs display BV-oxygenation activity. We also showed that MymA displays a distinctive substrate preference that we further investigated by kinetic parameter determination and that correlates with *in silico* modeling. We provide insights into distribution of BVMOs and the structural basis of their substrate profiling, and we discuss their possible redundancy in *M. tuberculosis*, raising questions about their versatility in prodrug activation and their role in physiology and infection.

IMPORTANCE Tuberculosis (TB), caused by *Mycobacterium tuberculosis*, is one of the leading causes of death worldwide. The rise in drug resistance highlights the urgent need for innovation in anti-TB drug development. Many anti-TB drugs require bioactivation by Baeyer-Villiger monooxygenases (BVMOs). Despite their emerging importance, BVMO structural and functional features remain enigmatic. We applied a comprehensive bioinformatic analysis and confirmed the presence of six BVMOs in *M. tuberculosis*, including MymA, EthA, and Rv0565c—activators of the second-line prodrug ethionamide—and the novel BVMO Rv0892. Combining *in silico* characterization with *in vitro* validation, we outlined their structural framework and substrate preference. Markedly, MymA displayed an enhanced capacity and a distinct selectivity profile toward ligands, in agreement with its catalytic site topology. These features ground the molecular basis for structure-function comprehension of the specificity in these enzymes and expand the repertoire of BVMOs with selective and/or overlapping activity for application in the context of improving anti-TB therapy.

Editor Christina L. Stallings, Washington University School of Medicine in St. Louis

Copyright © 2022 Tomas et al. This is an open-access article distributed under the terms of the [Creative Commons Attribution 4.0 International license](https://creativecommons.org/licenses/by/4.0/).

Address correspondence to Hedia Marrakchi, hedia.marrakchi@ipbs.fr, Gwenaëlle André, gwenaelle.andre@inrae.fr, or Anne Lemassu, anne.lemassu@ipbs.fr.

*Present address: Nguyen-Hung Le, Department of Molecular Microbiology, Washington University School of Medicine in St. Louis, St. Louis, Missouri, USA.

The authors declare no conflict of interest.

Received 28 May 2021

Accepted 2 February 2022

Published 17 March 2022

KEYWORDS tuberculosis, mycobacteria, monooxygenase, BVMO signature, modeling, substrate selectivity, protein structure-function

Tuberculosis (TB) caused by *Mycobacterium tuberculosis* remains a major health problem worldwide with 10 million people infected and more than 1.5 million deaths per year (1). Despite the existence of antibiotics and a vaccine, the treatment of TB remains complex, especially in the context of comorbidity factors such as coinfection with human immunodeficiency virus (HIV)/AIDS, the recent SARS-CoV-2 virus, diabetes, and broader determinants such as poverty, undernutrition, and poor access to cures in low-income countries. The emergence of multidrug-resistant TB (MDR-TB) and extremely resistant TB (XDR-TB) adds to this global health issue. Therefore, there is an urgent need to develop new anti-TB drugs that would shorten the therapy duration, improve efficacy against MDR-TB, and enable administration of drug combinations with antiretroviral agents.

One strategy to accelerate development of anti-TB compounds is based on exploiting molecules and mechanisms whose effectiveness is already established. Among the drugs known to be effective, several must be bioactivated by *M. tuberculosis* to become highly toxic to the pathogen. This is particularly the case for ethionamide (ETH), isoxyl (ISO), and thiacetazone (TAC), known anti-TB prodrugs, but also newly identified compounds active against *M. tuberculosis*; all are activated through oxidation by a peculiar class of monooxygenases, the Baeyer-Villiger monooxygenases (BVMOs) (2, 3). Indeed, the *M. tuberculosis* genome includes at least three BVMO genes that can activate ETH: *rv3854c* (also known as *ethA* for ETH activator) (4), *rv3083* (also known as *mymA*) (5), and *rv0565c* (6). EthA and MymA are both type I BVMOs, which means that they both harbor a Rossmann fold and are dependent on flavin adenine dinucleotide (FAD) cofactor and NADPH electron donor (7). Moreover, both enzymes have been recognized as important for developing anti-*M. tuberculosis* inhibitors with improved efficacy and reduced toxicity (3, 5). Phenotypic analyses of *ethA* and *mymA* deletion mutants strongly indicate their involvement in lipid metabolism, including metabolism of mycolic acids (8–10). Also, the *mymA* operon is required for proper cell envelope ultrastructure and ability to survive inside activated macrophages (9). Yet, the prevalence and distribution of BVMOs in mycobacteria are still unknown, and their physiological function has not been explored in depth. Thus, it is of interest to identify and profile structurally and functionally the BVMOs of this phylum.

Here, we conducted a systematic bioinformatic analysis of 12 actinobacterial genomes, including those from mycobacterial species (*M. tuberculosis*, *M. leprae*, *M. smegmatis*, *M. bovis*, *M. marinum*, enlarged to *M. phlei*, and *M. vaccae*) and the *Mycobacteriales* order (*Corynebacterium glutamicum*, *Nocardia farcinica*, *Rhodococcus jostii*, *Mycolicibacterium gilvum*, and *Hoyosella subflava*) to characterize prevalence and distribution of type I BVMOs. Among the six putative BVMOs distributed along the phylogenetic tree in *M. tuberculosis*, we selected the candidate BVMOs Rv0565c and Rv0892, which exhibited sequence and structure similarity to MymA and EthA, as supported by homology modeling and substrate docking. The *in silico* results were further confirmed by *in vitro* assays, which showed that all four BVMOs can accommodate a variety of molecules. If Rv0892 is the most restricted enzyme in regard to substrate selectivity, Rv0565c, EthA, and MymA evidence a rather similar substrate profiling, with a particularly effective activity for MymA onto ethyl 3-oxohexanoate (Et3-ox). Such substrate acceptance is discussed in terms of sequence/structure features and promiscuity required for enzyme evolution as well as overlapping activity for application in the context of improving anti-TB therapy.

RESULTS

Sequence analysis and three-dimensional (3D) structure of *M. tuberculosis* BVMOs. In order to gain insight into prevalence and distribution of BVMOs in *M. tuberculosis*, we conducted a bioinformatic analysis for 12 actinobacteria and two reference genomes (*Escherichia coli* and *Bacillus subtilis*), with accession genomes listed in Fig. 1A.

The numbering of BVMOs is reported in Fig. 1A, and details of the identification are available on the GitHub page (https://smartbioinf.github.io/BVMO_type1_Tomas_et_al_2021/). The identified sequences strictly display the hallmark of BVMO, which is composed of BVMO1 and BVMO2 fingerprints [GA]GxWx₄[FY]P[GM]x₃D and FxGx₃Hx₃W[PD], respectively, encompassed by 2 Rossmann motifs composed of GxGx₂[GA]. Markedly, we implemented a visualization pipeline which evidences that the BVMO2 fingerprint is the limiting motif and could be considered a super-hallmark of type I BVMOs (Fig. 1A) (https://smartbioinf.github.io/BVMO_type1_Tomas_et_al_2021/). In other words, the observation of BVMO2 confirms the presence of the other motifs and thus certifies the existence of a BVMO enzyme. In addition, our analysis showed that *M. tuberculosis* counts 6, *M. vaccae* counts 12, and *Rhodococcus jostii* counts 8 putative type I BVMO candidates, whereas *E. coli*, *B. subtilis*, and *C. glutamicum* genomes have none (Fig. 1A). In *M. tuberculosis*, the six BVMOs, identified by sequence mining and confirmed by structural assessment, are the previously characterized BVMOs EthA and MymA, plus additional Rv1393c, Rv0565c, Rv0892, and Rv3049c candidates (Fig. 1B). Interestingly, EthA is the most largely conserved BVMO in the set of selected actinobacteria, with its presence in all genomes that contain BVMOs, and especially in *M. leprae*, which contains only one BVMO (Fig. 1A). Also, out of the four additional *M. tuberculosis* BVMOs, the annotated monooxygenase Rv0565c has an activity recently shown to confer susceptibility to ethionamide (ETH) and its analog prothionamide (PTH) (6). Rv0892, Rv1393c, and Rv3049c are annotated in UniProt as probable monooxygenases. Accordingly, the phylogenetic tree highlights that EthA, MymA, and Rv0565c cluster on the same branch, while Rv0892 is located separately, on another clade, and Rv1393c and Rv3049c are positioned even further away on more remote branches (Fig. 1B). Also, among the 6 BVMOs, EthA, MymA, Rv0565c and Rv0892 display (i) a probability of 100% to share structural homology with TmCHMO (*Thermocristum municipale* CycloHexanone MonoOxygenase a type I BVMO), (ii) an e-value below 1.e-15, and (iii) an alignment core of minimum 300 residues (Fig. 1C). Reversely, Rv3520c, primarily pulled out because it displays two Rossmann motifs, was not selected *in fine* because it contains none of the BVMO motifs (see Fig. S1A in the supplemental material). Nevertheless, to challenge it as a true negative, it was kept for later experimental validation (Fig. S1B). For all those reasons, we focused our *in silico* analysis on EthA, MymA, Rv0892, and Rv0565c proteins.

Homology modeling and substrate profiling of *M. tuberculosis* BVMOs. In order to assess how EthA, MymA, Rv0565c, and Rv0892 fold into a type I BVMO structure, and how they accommodate NADPH and FAD cofactors, we built a homology model for each protein, with TmCHMO as the template (PDB ID 5M10) (Fig. 2A). The catalytic dyad is formed by the strictly conserved aspartate residue, which belongs to the BVMO1 motif, and by a conserved arginine residue that does not belong to any conserved motif (red stars in Fig. 1C). Expectedly, the signature sequence motifs arrange similarly in 3D, bind cofactors FAD and NADPH, and participate to form the active site (Fig. 2B). As they are all located on the N-terminal side of the structure, this part of the active site is conserved. Reversely, the C-terminal part of the protein concentrates the differences in sequences, as overall similarity compared to TmCHMO decreases from 40% to 31%, 30%, and 21% for Rv0892, Rv0565c, EthA, and MymA, respectively. Among the main discrepancies which can be highlighted, one can note that F279, F434, and T435, highlighted as purple stars in Fig. 1C, are located in insertions in TmCHMO and that W492 is conserved only in Rv0892 with W448 (Fig. 2B and C). Interestingly, these substitutions locate at the junction between the substrate tunnel and the active site (11). Indeed, the TmCHMO junction site is composed of residues F279, F434, T435, W492, and F507, which could be responsible for a steric barrier and could act as gatekeepers to accept substrates or not. With V387, F390, W448, and F461, Rv0892 keeps almost all large and hydrophobic residues at these positions (Fig. 2B and C). Conversely, these residues are much less conserved in Rv0565c, EthA, and MymA, and when substituted in three out of five residues, they are replaced by smaller or even polar residues (Fig. 2C). Their substitutions into smaller residues or even

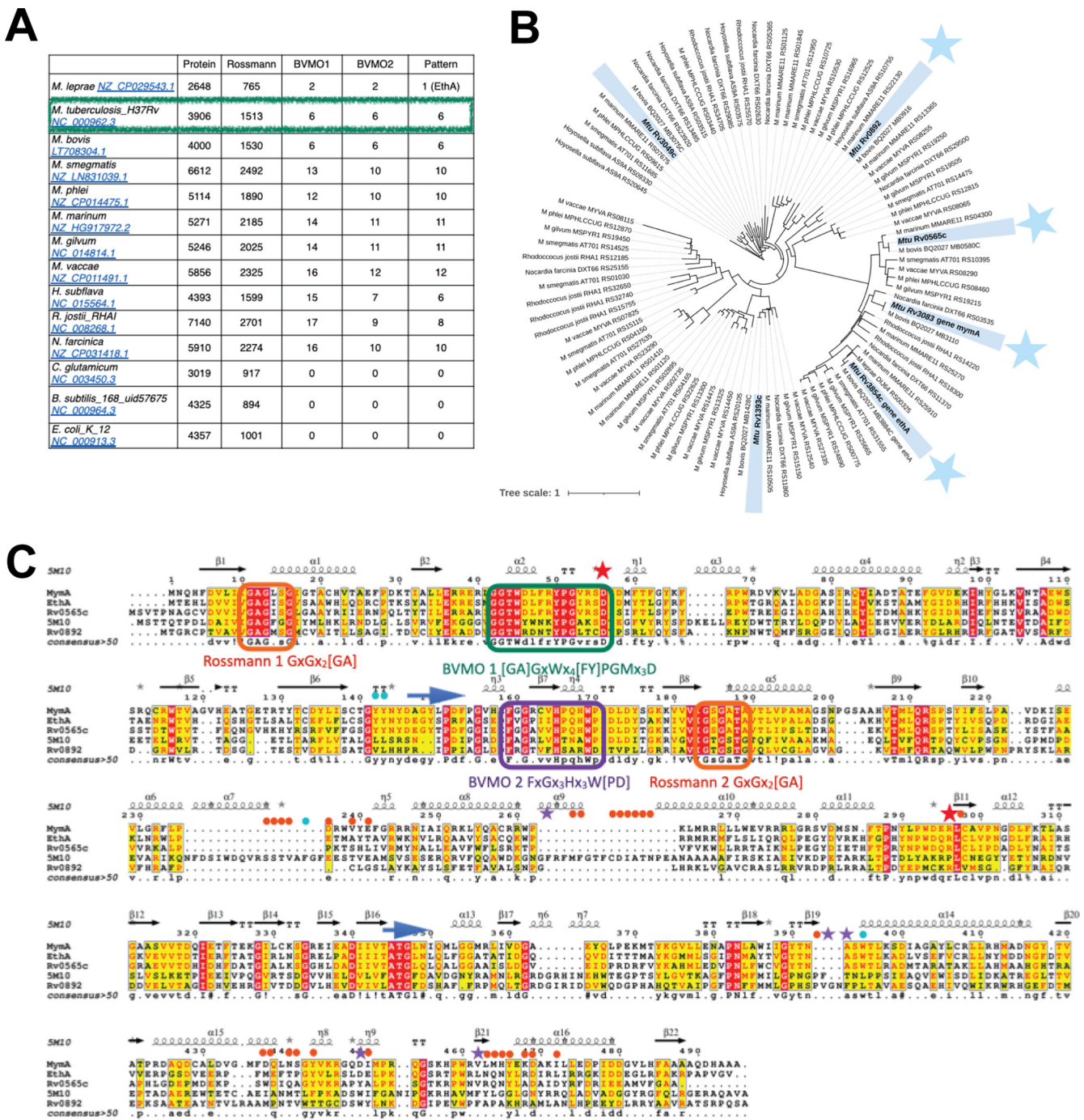


FIG 1 Distribution and structural features of BVMOs. (A) Cooccurrence of motifs that form specific fingerprints and characterize type I BVMOs as observed within 12 actinobacterial and selected Gram-positive and Gram-negative reference genomes. Fingerprints have been identified using FuzzPro (EBI) and in-house interactive visualization implemented under the COSP workflow (<https://github.com/SmartBioInf/COSP>). (B) Phylogenetic tree from the putative type I BVMO using NGPhylogeny and iTOL. (C) Multiple alignment of the four selected BVMOs with the 3D template *TmCHMO*, using ClustalW and ESPrT. The pattern motifs contoured in orange, deep teal, and purple are Rossmann 1 and 2, BVMO1, and BVMO2, respectively. The catalytic aspartate and arginine residues are marked with red stars, and the residues that define the active site are highlighted with a cyan circle, while the ones that define the substrate tunnel have a solid orange circle, and those that could restrict the entrance between the substrate tunnel and the active site are highlighted with a purple star. The two blue arrows define the hinge linkers that connect the FAD and NADPH domains and are involved in domain rotation.

their absence could result in a distinct substrate selectivity profile. Thus, one can hypothesize that these discrepancies could act on substrate acceptance and contribute to distinct binding profiles. Altogether, these data led to the hypothesis that the four *M. tuberculosis* monooxygenases could share a similar reaction mechanism, while they likely differ in

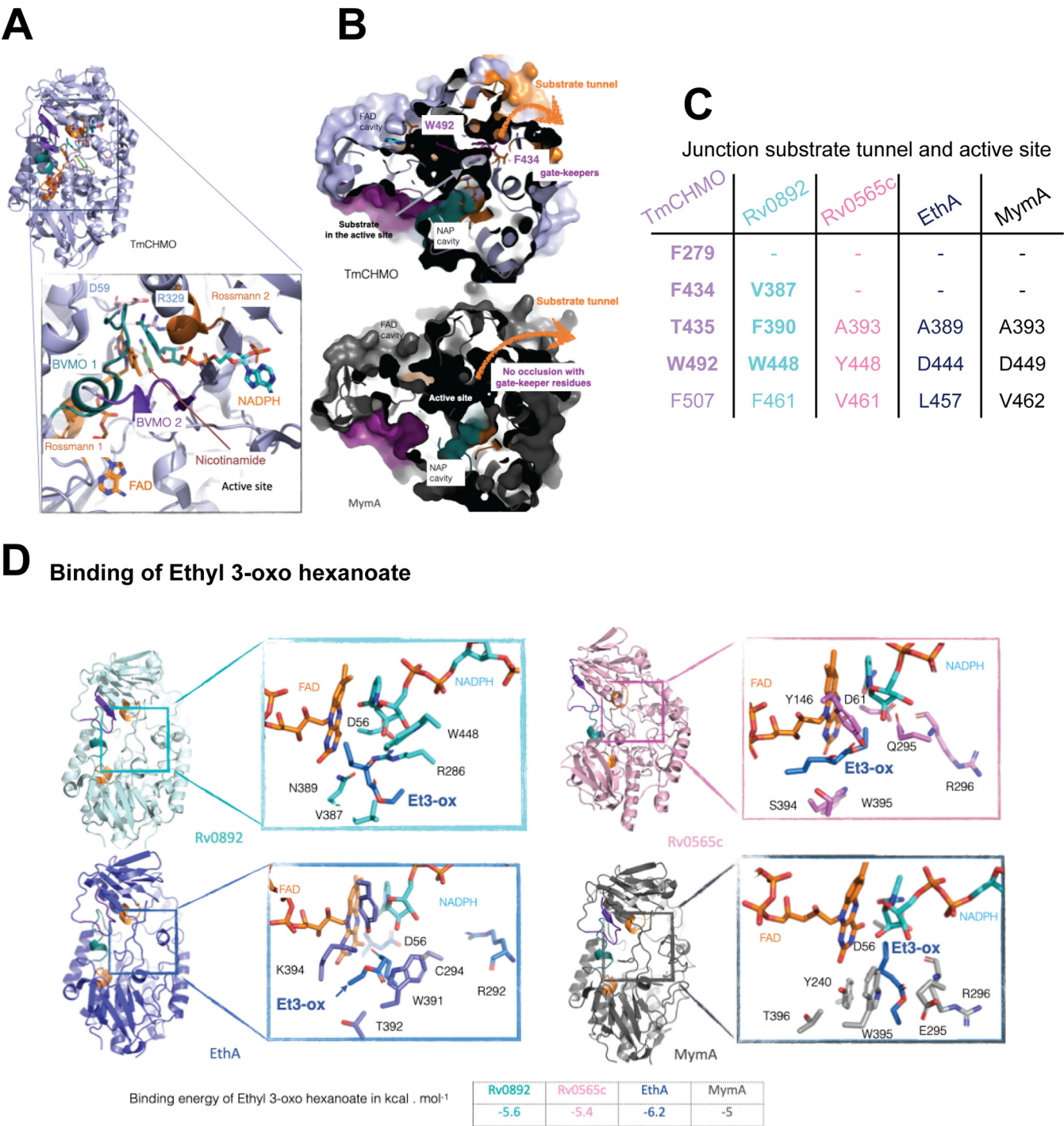


FIG 2 Homology modeling of *M. tuberculosis* BVMOs. (A) Mapping of BVMO fingerprints onto the 3D structure of *TmCHMO*. The fingerprints have the same color code as in Fig. 1C, with Rossmann 1 and 2 colored in orange, and BVMO1 and BVMO2 colored in deep teal and purple, respectively. Inserted below is a close view of the active site, with the binding of FAD and NADPH cofactors. The catalytic residues D59 and R329 are shown as sticks. (B) Surface cross section of *TmCHMO* and *MymA*. In the former, the accessibility of ligands could be sterically hampered by a restraint at the junction between the substrate tunnel and the catalytic site, possibly due to gatekeeper residues composed of F279, F434, and W492. Conversely, in *MymA*, the active site is openly accessible directly through the substrate tunnel as no residues hamper the junction between the substrate tunnel and the catalytic site. (C) Table with the listing of residues that form the junction between the substrate tunnel and the active site for the four modeled enzymes. From Rv0892 to *MymA*, the residues are progressively fewer and smaller, so one can hypothesize that atomic hindrance could play for substrate selectivity through a steric gradient from restricted for Rv0892 to relaxed for *MymA*. (D) Homology modeling of Rv0892, *MymA*, *EthA*, and Rv0565c. Inserted are close views of the docking of ethyl 3-oxohexanoate with details of residues involved in binding as well as a table of binding energy in kilocalories . mole⁻¹.

their substrate selectivity. To challenge that assumption, we performed *in silico* docking and then *in vitro* enzymatic studies.

To establish the substrate profiling and evaluate the substrate preferences of the four enzymes, four ligands mimicking either cyclic or linear substrates were docked in each active site, and their interaction energy was computed accordingly. The best pose, among the 10 runs performed for each pair of protein and ligand and with respect to the interaction energy, was kept. As shown for the ethyl 3-oxohexanoate (Fig. 2D) and more largely for the panel of ligands, the affinity is comparable for any combination of enzyme and ligand, ranging from -4.5 to -6.2 kcal · mol⁻¹ (Table S2). From our point of view, such discrepancy in interaction energy is not significant enough to assess a strict preference, whether it concerns enzyme or substrate. It is important to acknowledge that a docking is a pose of a molecule once captured within the cavity pocket and not its behavior along the diffusion pathway. This point is particularly relevant when considering not only the binding of the small molecule but its accessibility to reach the reactive center, as well as its capacity to trigger enzyme motion and conformational change to accommodate a substrate. Indeed, the discrepancies in sequences are mapped in the structure partly within the close vicinity of the so-called N-terminal hinge linker (I151-D153 *TmCHMO* numbering) but mostly within the C-terminal domain (Fig. 1C). The first segment, along with the second linker hinge, which is more conserved, A379-G381 (*TmCHMO* numbering), could be involved in domain rotation, upon ligand binding. This has already been described for a similar topology domain of thioreductases (12). Moreover, the second series of substitutions impacts mostly residues involved in the substrate tunnel. Particularly, they concentrate at the junction formed by the end of the tunnel and the entrance to the active site; those residues are highlighted as orange spots in Fig. 1C and depicted as orange surface in Fig. 2B (13).

Taken together, homology modeling and substrate docking validate that the four proteins should be BVMO enzymes. They possess the 3D fold typical of this class of enzymes, accommodate both cofactors and ligand, and eventually prime the very first shell of catalytic residues as ready for oxidation. In addition, *in silico* characterization addresses the point that differences on sequences could impact NADPH domain motion and substrate acceptance; especially, discrepancies along the substrate tunnel could tune the substrate profiling. It also emphasizes that Rv0892 is closer to *TmCHMO* with respect to gatekeeper residues and hinge N-terminal linker. From Rv0892 to MymA, the residues are progressively fewer and smaller, so one can hypothesize that substrate selectivity, based on steric bulk from restricted for Rv0892 to relaxed for MymA, could tune the accessibility from outside. To conclude, Rv0892 and *TmCHMO* should partake in substrate profiling, sensitively distinct from Rv0565c, EthA, and MymA, which could overlap substrate profile similarity, due to closer sequences and comparable 3D arrangement. Therefore, we expect that Rv0892 will catalyze oxidation of similar substrates as those of *TmCHMO*, while Rv0565c, EthA, and MymA could line up similar substrate profiling behavior, with subtle specificity due to residue substitutions (i.e., highlighted as blue arrows, solid orange circles, and purple stars in Fig. 1C).

Purification and substrate selectivity profiles of *M. tuberculosis* BVMOs. In order to gain knowledge into the possible function and putative distinctive substrate selectivity of MymA, EthA, Rv0565c, and Rv0892, we overexpressed and optimized purification of the four proteins. Except for the reported purification of EthA (14, 15), previous reports in the literature described either assaying activity using crude extracts overexpressing *M. tuberculosis* BVMOs (16) or unsuccessful attempts to purify the proteins, likely due to their low solubility in classical expression systems (6).

We cloned the four corresponding genes into *E. coli* pET expression plasmids (Table S1) and performed multiple expression and purification optimization assays. All attempts to express Rv0565c and Rv0892 under soluble forms were unproductive whereas we succeeded in purifying MymA_{coli} and EthA_{coli} proteins to homogeneity and with relatively good yields (Fig. S2A).

To comparatively dissect the substrate preferences of all selected BVMOs, we therefore implemented an optimized expression and purification workflow in the mycobacterial host strain *M. smegmatis*, already successfully used as an efficient surrogate host to express *M. tuberculosis* proteins (17). Indeed, expression of the four recombinant 6×His-tagged BVMOs in *M. smegmatis* allowed their significant enrichment, as evidenced by stain-free analysis and immunodetection (Fig. S2B).

Despite the low purification yields in this expression system, we were able to investigate the *in vitro* activity of the four proteins in the presence of selected aliphatic and cyclic substrates. The assay designed to assess the BVMO activity consisted in following the NADPH oxidation coupled to monooxygenation of the substrate, as previously described (18) (Fig. 3A). Validation of the spectrophotometric assay was performed using commercial CHMO and the non-BVMO Rv3520c as positive and negative controls, respectively (Fig. S1B). Notably, these results reinforce the strength of our *in silico* strategy to distinguish between BVMO and non-BV monooxygenases (Fig. S1A).

All purified BVMOs were assessed for their activity, by checking that the measured NADPH oxidation is dependent upon—and proportional to—enzyme concentration (protein dose-response curve), as exemplified by MymA (Fig. 3B). The four purified proteins were then assayed under the same experimental conditions, in biological and technical replicates in the presence of the molecules 2-octanone (2-oct), thioanisole (ThioA), ethyl 3-oxohexanoate (Et3-ox), and cyclohexanone (CH).

All four BVMOs display a Baeyer-Villiger oxygenase activity and similar substrate profiles, with 2-oct and Et3-ox being the most effective substrates. A similar experimental substrate profiling can be noted for Rv0565c, EthA, and MymA with limited to marked increasing oxidation from cyclic to linear substrate (Fig. 3C). Particularly, Rv0565c and EthA are efficient in oxidizing 2-octanone while MymA is very active on ethyl 3-oxohexanoate. Rv0892 exhibits markedly low catalytic rates on the tested substrates (specific activities, 27 nmol.min⁻¹.mg⁻¹ for Et3-ox and 23 nmol.min⁻¹.mg⁻¹ for 2-oct); nevertheless, its activity shows that it is a BVMO enzyme (Fig. S3).

EthA and Rv0565c seem to prefer 2-oct to Et3-ox (Fig. 3C) over the cyclic substrates; however, analysis of variance (ANOVA) and *post hoc* tests could not provide sound statistical proof for this difference (Fig. S4). Most notably, though, a robust proof of the opposite activity pattern was produced for MymA, which presents significantly higher activity with Et3-ox compared to 2-oct.

Assay adaptation and enzymatic characterization of MymA. In order to gain further insights into MymA enzymatic properties with regard to its distinctive substrate profile and given the increasing interest in this anti-TB prodrug activator, we miniaturized the BVMO assay using purified MymA_{coli} enzyme for which we obtained pure protein and high-purification yields (1.7 mg/L culture [Fig. S1A]). We first checked its activity compared to that of the protein produced in *M. smegmatis*. Indeed, MymA_{coli} was active in the presence of Et3-ox (Fig. S5A). We then set up a microplate assay for NADPH oxidation to follow the BVMO activity and showed that comparable specific activities for MymA_{coli} were obtained using either a cuvette or a 96-well plate format (Fig. S5B).

Using the microplate assay and MymA_{coli} we therefore determined the catalytic constants for Et3-ox and 2-oct (Fig. 4A). The steady-state apparent parameters indicate higher catalytic constants (k_{cat}) for Et3-ox (0.88 ± 0.03 s⁻¹) compared to 2-oct (0.11 ± 0.01 s⁻¹) and catalytic efficiency (k_{cat}/K_M), while the K_M (Michaelis constant) values are marginally comparable for the two substrates (0.24 ± 0.04 mM and 0.4 ± 0.1 mM, respectively). The measured kinetic parameters are on the same order as those obtained for other BVMO-substrate pairs previously characterized (11, 18). This could correlate with docking analysis which shows that Et3-ox and 2-oct ligands engage similar binding energy with MymA. However, the best poses for 2-oct and Et3-ox evidence a difference in the side chain rotamer of E295, located within the first catalytic shell of protein residues. Such rotation of E295 could favor a polar interaction of Et3-ox both with the backbone of the catalytic R296 and with the side chain of W395 (Fig. 4B).

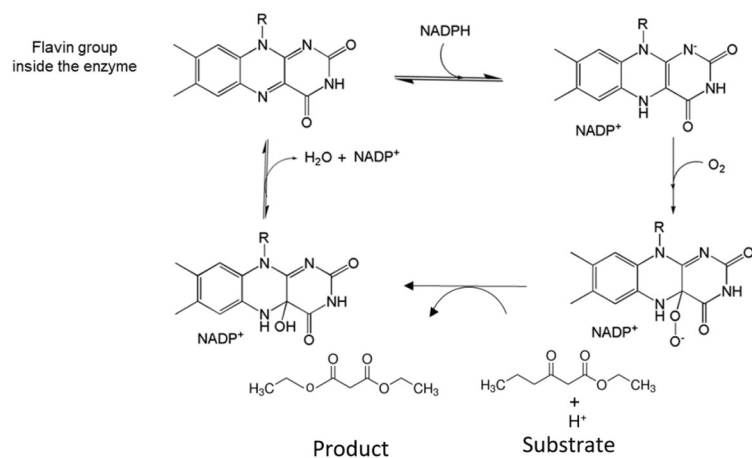
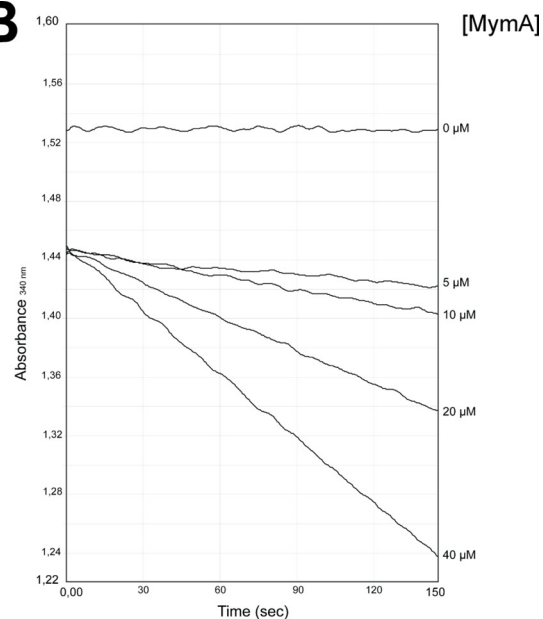
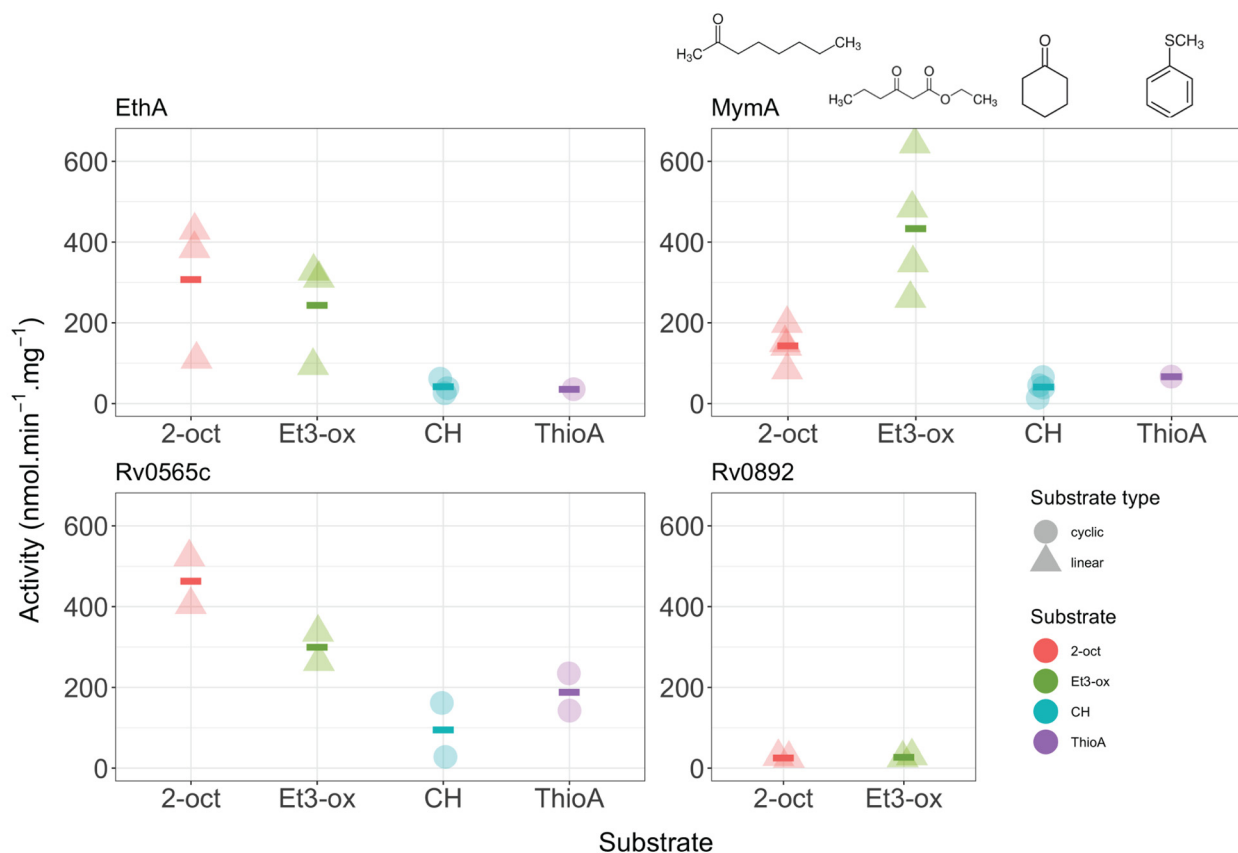
A**B****C**

FIG 3 *In vitro* BVMO assay and substrate profiling. (A) Catalytic mechanism of BVMO with the different oxidation states of the FAD. (B) Kinetics of NADPH oxidation at 340 nm in the presence of MymA. The reactions were carried out for 4 min at 25°C with 5 mM ethyl 3-oxohexanoate (Et3-ox) as the substrate and started by addition of increasing concentrations of MymA, as described under Materials and Methods. (C) Activity of EthA, MymA, Rv0565c, and Rv0892, in the presence of various substrates: cyclohexanone (CH), thioanisole (ThioA), ethyl 3-oxohexanoate (Et3-ox), and 2-octanone (2-oct). Enzyme concentration in the assay was 10 to 40 μg/mL, the substrates were used at 5 mM (1 mM for thioanisole) and NADPH was used at 0.2 mM. Activity rates correspond to nanomoles of NADPH consumed per minute per milligram of protein for each BVMO. Circles represent the mean values for at least two protein extraction replicates for a given independent experiment.

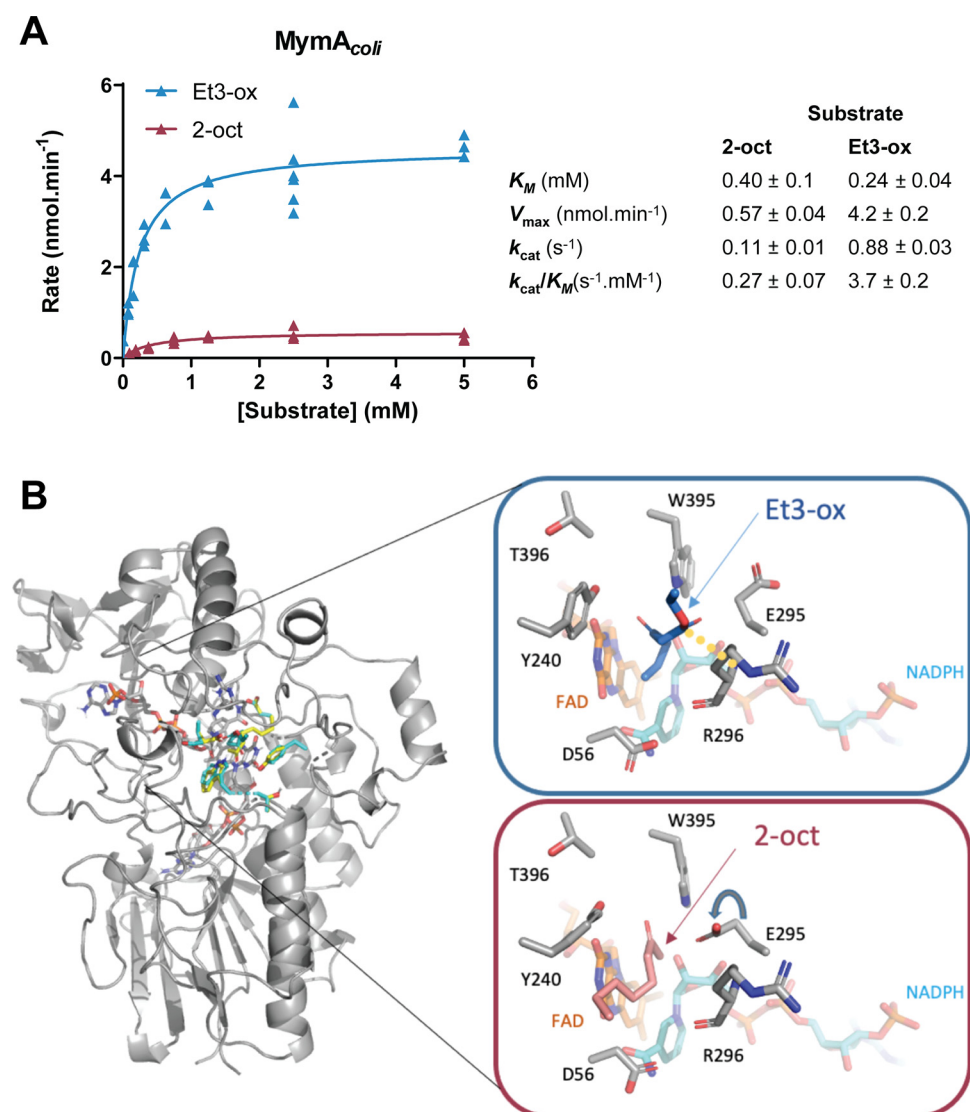


FIG 4 MymA substrate selectivity. (A) Steady-state kinetics of MymA produced in *E. coli* (MymA_{coli}) with ethyl 3-oxohexanoate (Et3-ox, blue triangles) and 2-octanone (2-oct, red triangles). Activities were determined at 25°C by following the NADPH consumption in 96-well microplates, in a 250- μ L volume. Reaction mixtures contained 0.5 mM NADPH and increasing concentrations of the substrate (0 to 5 mM) and were started by addition of MymA_{coli} at 20 μ g/mL. Data were fitted to the Michaelis-Menten equation, and kinetic parameters for Et3-ox and 2-oct were determined using GraphPad Prism 5.04. (B) Docking of Et3-ox and 2-oct on MymA, in blue and salmon, respectively. Inset is a closeup view of the binding. The rotation of E295 is shown by a gray arrow, and the polar bond between the ligand and R296 is highlighted by a yellow dashed line.

DISCUSSION

In this work, we implemented an original bioinformatic pipeline, based on sequence mining and structural homology detection, not only to identify but also to visualize type I BVMOs. As a first main result, our bioinformatic pipeline was experimentally confirmed as accurate in identifying type I BVMOs in a series of genomes. It also evidenced that cooccurrence of two Rossmann motifs, plus BVMO1 and BVMO2 fingerprints, is required to form the hallmark characterizing type I BVMOs. Markedly, our bioinformatic analysis highlights that when BVMO2 is present, all other specific motifs are also present, which suggests that BVMO2 could define a “super” motif to screen for BVMO in entire genomes. Interestingly, this motif can eventually be degenerated (data not shown). Last, while the BVMO2 fingerprint is not strictly part of the active site, it belongs to the linker segment that connects the FAD-binding domain to the NADPH-binding domain of these

monooxygenases (19). In line with that, Rv3520c, which harbors only two Rossmann motifs, was shown to be strictly inactive.

As a second result, we found BVMOs in all but one of the screened genomes of *Mycobacteriales*, which is *C. glutamicum*. The number of identified BVMOs present within these genomes varied from one, in *M. leprae*, which is EthA, to up to 12 in *M. vaccae*. For *M. leprae*, this is fully consistent with the work of Fraaije et al. (18). Also, we counted no fewer than 8 to 12 putative BVMOs for *M. phlei*, *M. vaccae*, *R. jostii*, or *N. farcinica*. Those bacteria are known to thrive in a broad range of environments, including soil, water, and eukaryotic cells. Also, they have large genomes. This broad distribution of BVMOs is likely attributable to the diversity of carbon sources available for these organisms. As BVMOs catalyze key reactions in metabolic pathways, the primary metabolism of atypical carbon sources could confer an adaptative behavior and an evolutionary advantage (7). These enzymes can adapt to a wide range of ketones as substrates to oxidize them into esters or lactones (7). Despite this physiologic redundancy, the majority of newly identified potential BVMOs remain to be formally functionally annotated and biochemically characterized in future studies.

We then focused on the human pathogen *M. tuberculosis*, which encodes 6 BVMOs as confirmed in our analysis. Earlier studies have demonstrated that *M. tuberculosis* uses two of these BVMOs, EthA and MymA, to activate ETH, highlighting their importance for the pharmacological mechanism of this class of TB drugs (3–5, 20, 21). Later it was shown that some other proteins, including Rv0565c, can also activate this drug (6). Our current analysis suggested that monooxygenase-annotated gene product Rv0565c represents a BVMO with structure and function similar to EthA and MymA, while Rv0892 could be closer to a regular cyclohexanone BVMO. We followed up analysis on testing this hypothesis. Our homology modeling revealed that all four enzymes are structural homologues, with local mutations mapped mainly within the substrate tunnel, likely impacting substrate accessibility rather than expected binding preference. Formerly, the substrate tunnel was suspected to select and drive ligands to the active center and expel products once oxidized. We docked a series of putative substrates (cyclic and aliphatic molecules) into homology models and observed that indeed all four enzymes share a similar binding behavior with respect to their interaction energy with ligands. Nevertheless, we could highlight some insertions or substitutions along the so-called substrate tunnel and at the entrance of the active site that could impact the destiny of the ligands. We also identified subtle mutations at the first hinge linker that is known to contact both BVMO1 and -2 motifs. This double-hinge β -sheet linker is conserved in Baeyer-Villiger monooxygenases, where it is suspected to be involved in domain motion. Possibly, substitution could act on NADPH domain motion, but at this stage, this assumption would need to be better documented. From *in silico* analysis and comparison with *TmCHMO*, gatekeeper residues are more conserved in Rv0892 than in Rv0565c, EthA, and MymA. Thus, we hypothesize that Rv0892 could share a compact cavity similar to *TmCHMO* and distinct from Rv0565c, EthA, and MymA; all three would gather in a similar topology (13, 22). This is relevant with respect to the phylogeny tree. To challenge this hypothesis, we further performed *in vitro* assays. They confirmed that Rv0892 behaves differently from Rv0565c, EthA, and MymA, which exhibit comparable enzyme activities and substrate specificities. Rv0565c, EthA, and MymA share *in vitro* a similar substrate profile, with respect to their tropism for the linear substrates 2-oct and Et3-ox. Markedly, MymA displays a distinct effective behavior when the linear substrates are considered. Reversely, Rv0892 is much less active on those substrates. In-depth investigation of Rv0892 behavior toward the cyclic substrate was hampered by very low protein yields and extremely low substrate conversion rates under assay conditions. Future purification and assay optimizations will be required to assess the ability of Rv0892 to oxidize CH and ThioA. Altogether, this work confirms that Rv0565c, EthA, and MymA are *M. tuberculosis*

BVMOs and identifies Rv0892 as a new BVMO, with a likely distinct substrate selectivity that remains to be ascertained. Still, for *M. tuberculosis* we need to correlate BVMO substrate profiling with their physiological relevance within the cell, which is beyond the sole capacity to activate prodrugs. Open questions remain as to the versatile role of these *M. tuberculosis* BVMOs and their possible involvement in lipid metabolism (9).

Given that BVMOs are able to oxidize a broad spectrum of substrates, they likely exhibit some physiological redundancy. Therefore, we suggest that the presence of multiple BVMOs would allow an organism to readily adapt to a wide range of carbon sources. From this perspective, it is important to pursue the efforts and expand our knowledge of BVMO function with the ultimate goal of developing strategies for controlling and exploiting this class of enzymes in the context of anti-TB drug development.

MATERIALS AND METHODS

Bioinformatic analysis. The genomes of mycobacteria, from *M. tuberculosis*, *M. leprae*, *M. smegmatis*, *M. bovis*, *M. marinum*, *M. phlei*, and *M. vaccae*, and the genomes of corynebacteria, from *C. glutamicum*, *N. farcinica*, *R. jostii*, *M. gilvum*, and *H. subflava*, were selected and downloaded from the NCBI site. The references Gram-positive *Bacillus subtilis* and Gram-negative *Escherichia coli* were also included. Every sequence of each genome was screened with the EMBOSS FuzzPro tool, to search for sequence motifs that display the hallmarks for type I BVMOs (23, 24). Such a sequence pattern contains two GxGx₂[GA] motifs, so-called Rossmann ones, a [GA]GxWx₄[FY]P[GM]_x₃D motif named here BVMO1, and a FxGx₃Hx₃W[PD] motif named here BVMO2, where the residues inserted in the brackets show the possible substitutions. With respect to the BVMO type I enzymatic signature, sequences that strictly associate fingerprints in the following order were kept: Rossmann motif-BVMO1-BVMO2-Rossmann motif. A dedicated bioinformatic pipeline was developed to identify readily all type I BVMOs within entire genomes. The pipeline, implemented to deliver an interactive comparison among a series of genomes, is available on GitHub (<https://github.com/SmartBioInf/COSP>). A phylogenomic analysis was performed on selected sequences with the FastME/OneClick workflow of NGphylogeny software (<https://ngphylogeny.fr/>) (25), and the resulting tree was visualized using iTOL (Interactive Tree Of Life; <https://itol.embl.de>) (26). Then, the sequences were computed with HHpred, using the default parameters and the structural database PDB_mmCIF70, to detect their structural homologues and assess if they all display the same 3D fold (27). In *M. tuberculosis*, the sequences that (i) retain pattern detection; (ii) show 100% probability of being structurally homologous to the template, cyclohexanone BVMO from *Thermococcus municipale* (TmCHMO) chosen upon HHpred; and (iii) distribute evenly on the phylogeny tree were selected for *in silico* and then *in vitro* characterization. Namely, these are Rv0892, Rv0565c, Rv3083 (MymA), and Rv3854c (EthA). For the sake of clarity, Rv3083 and Rv3854c are named here MymA and EthA, respectively.

Homology modeling of full-length Rv0565c, Rv0892, MymA, and EthA. Rv0892, Rv0565c, MymA, and EthA were homology modeled using TmCHMO as the 3D template because it is one of the closest structural homologues identified by HHpred (27). Also, TmCHMO is in complex with FAD, NADPH, and nicotinamide (5M10 PDB ID) (22). The model-building software Modeller was chosen (version 9.18) (28) starting from a multiple alignment of the four proteins plus the reference template, using the ClustalW algorithm for its accurate precision (with default parameters) (29) and subsequently using ESPrpt for its capacity to insert the secondary structure elements of the template (30). For each protein, 100 homology models were generated, the final structure that associates the lowest values of Modeller function and DOPE score was selected, and the stereochemistry was checked using MolProbity (31). Finally, the cofactors were added and each complex was minimized to relax local probable steric clashes, using Gromacs Charmm36 forcefield with the steepest-descent algorithm (32).

Docking of ligands. The molecule of nicotinamide was redocked in the binding pocket of TmCHMO, to check if the protocol docks it similarly to its position in the crystal structure. As its pose was confirmed, it served as a positive control, and then the protocol was approved for subsequent docking of ligands in the binding sites of the homology-modeled Rv0892, Rv0565c, MymA, and EthA proteins. AutoDock tools were used, with a grid box centered on the crystal position of the nicotinamide and the genetic algorithm of Lamarck (33). The side chains of residues located within 4 Å from the nicotinamide were allowed to be flexible so that rotamer transition could be allowed. With anticipation, the grid box was sized to accommodate the largest ligand of the series, which was composed of cyclohexanone, thioanisole, 2-octanone, and ethyl 3-oxohexanoate. When proper, their dihedral angles were set free to rotate. Subsequently, each ligand was docked in the binding site of every BVMO protein, using similar docking parameters, so that resulting binding energies could be compared. For each ligand, the complex showing the best affinity between ligand and protein, i.e., the lowest binding energy computed in kilocalories · mole⁻¹, was selected for molecular analysis. Finally, apo and holo models were visually inspected using PyMOL 2.0.7 (Schrödinger, LLC).

Plasmid construction. The *rv0892*, *rv3083* (*mymA*), and *rv3854c* (*ethA*) genes were cloned into the isopropyl-β-D-thiogalactopyranoside (IPTG)-inducible mycobacterial expression vector pLD1 (17) or

pET28a using primers (see Table S1 in the supplemental material) designed to generate PCR product from the genomic DNA of *M. tuberculosis* strain H37Rv, containing the NotI/NdeI restriction sites for cloning into pLD1 or BamHI/HindIII for cloning into pET28a. The inserts were verified by sequencing (Eurofins Genomics, France). The *rv0565c* gene was cloned into the pV2 expression vector (34) using the primers designed to generate a PCR product corresponding to the entire *rv0565c* gene from *M. tuberculosis* strain H37Rv and harboring NdeI/HindIII restriction sites enabling direct cloning into the pV2 vector (Table S1). The insert was verified by sequencing (Microsynth, Switzerland).

Bacterial strains and culture conditions. For expression in *M. smegmatis*, the plasmids pLD1-*rv0892*, pLD1-*rv3083* (*mymA*), and pLD1-*rv3854c* (*ethA*) were electroporated into *M. smegmatis* mc² 155 GroELΔC. Transformants were selected on 7H10-0.2% glycerol agar plates with hygromycin B (100 μg/mL). Starter cultures were grown for 30 h at 37°C under shaking and then diluted in 2 L of 7H9 medium (Difco) supplemented with glycerol (0.2%), tyloxapol (0.025%), and hygromycin B (100 μg/mL). The resulting cultures were incubated under shaking (180 rpm) at 37°C until reaching an optical density at 600 nm (OD₆₀₀) of 0.6. BVMO overexpression was induced with IPTG (0.5 mM final concentration) (Euromedex, France). Cells were harvested 3 h after IPTG induction, pelleted by centrifugation, flash-frozen, and kept at −80°C.

For expression of *Rv0565c*, *M. smegmatis* GroEL1ΔC cells were transformed with pV2-*rv0565c* and cells were stored with 25% glycerol. A 100-mL starter culture of LB medium containing 0.05% Tween 80 and 20 μg/mL kanamycin was inoculated at 1:100 from the glycerol stock and grown at 37°C under agitation until reaching an OD₆₀₀ of ~1.5. Two-liter cultures in LB media containing 20 μg/mL kanamycin inoculated with 20 mL of the starter culture were cultivated for 48 h at 30°C under agitation. Cells were harvested by centrifugation, and pellets were washed with 25 mM Tris-HCl, pH 7.5, 300 mM NaCl.

For expression in *E. coli*, One Shot BL21 Star(DE3) chemically competent cells were transformed with pET28a-*rv3083* or pET28a-*rv3854c* and grown in 500 mL of LB medium supplemented with 50 μg/mL kanamycin at a temperature of 37°C under agitation. Induction was performed at an OD₆₀₀ of 0.6 by the addition of 50 μM IPTG for *MymA* or 250 μM for *EthA*. Cells were harvested after an overnight induction period at 16°C, pelleted by centrifugation, washed with phosphate-buffered saline (PBS) (Euromedex), and stored at −80°C.

Purification of recombinant *EthA* and *MymA* (produced in *E. coli*). Cell pellets (2 g, wet weight) were thawed and resuspended in 50 mL lysis buffer (50 mM HEPES, pH 7.0 for *MymA* or 50 mM sodium phosphate, pH 7.5, for *EthA*, both supplemented with 300 mM NaCl, 10 mM imidazole, 8% glycerol). One milligram/milliliter lysozyme, 0.1% Triton X-100, 1 mM AEBSF [4-(2-aminoethyl)benzenesulfonyl fluoride hydrochloride], and 1 mM dithiothreitol were also added in this lysis buffer. The suspension was lysed on ice with an Emulsiflex C5 homogenizer (Avestin) using 100,000-kPa pulses, and clarified lysate was obtained after centrifugation at 22,000 × *g* for 30 min. The clarified lysate was applied to a 1-mL HisTrap HP column (Cytiva) equilibrated with lysis buffer supplemented with 20 mM imidazole. Nonspecific bound proteins were eluted from the beads with lysis buffer supplemented with 90 mM imidazole. Proteins of interest were eluted with elution buffer (lysis buffer supplemented with 300 mM imidazole).

Eluted fractions were 10-fold concentrated using Vivaspin 20 (30-kDa cutoff; Cytiva), and 500-μL fractions were loaded at 0.5 mL/min on a Superose 6 Increase 10/300 GL (Cytiva) equilibrated with buffer (50 mM HEPES, pH 7.0 or 50 mM sodium phosphate, pH 7.5, 300 mM NaCl for *MymA* and *EthA*, respectively). The collected fractions were concentrated, and total protein concentration was determined using the bicinchoninic acid (BCA) protein assay kit (Sigma-Aldrich).

Purification of recombinant *EthA* and *MymA* (produced in *M. smegmatis*). Cell pellets (10 g, wet weight) were thawed and resuspended in 50 mL lysis buffer (50 mM sodium phosphate, pH 7.5, 300 mM NaCl, 8% glycerol) supplemented with 2 mM AEBSF. The suspension was lysed with a cell disruptor (One Shot model; Constant System Ltd., France) at 260,000 kPa. The clarified lysate obtained after centrifugation at 20,000 × *g* for 20 min was incubated with a volume of immobilized-metal affinity chromatography (IMAC) resin (Ni-NTA Agarose, Qiagen). After 2 h of incubation at 4°C, under agitation, the beads were recovered and washed with lysis buffer supplemented with 10 mM and then 60 mM imidazole. The fractions obtained upon elution with 300 mM imidazole were desalted on a PD10 Midi TrapG-25 column (Euromedex) and concentrated using a Vivaspin 20 (10-kDa cutoff; Sartorius).

Purification of recombinant *Rv0892* (produced in *M. smegmatis*). Cell pellets (10 g, wet weight) were thawed and resuspended in 50 mL lysis buffer (50 mM sodium phosphate, pH 7.5, 300 mM NaCl, 8% glycerol) supplemented with 1 mM AEBSF. The suspension was lysed with a cell disruptor (One Shot model; Constant System Ltd., France) at 260,000 kPa. The clarified lysate obtained after centrifugation at 20,000 × *g* for 20 min was injected on a 1-mL HisTrap HP column (Cytiva) and then washed with lysis buffer supplemented with 90 mM imidazole. The fractions obtained upon elution with 300 mM imidazole were desalted on a PD10 Midi TrapG-25 column (Euromedex) and concentrated using a Vivaspin 20 (30-kDa cutoff; Cytiva).

Purification of recombinant *Rv0565c* (produced in *M. smegmatis*). Cell pellets (20 g, wet weight) were resuspended in 30 mL lysis buffer (25 mM Tris-HCl, pH 7.5, 300 mM NaCl) and disrupted by sonication on ice (60 s on, 90 s off, 15 times, 1-cm probe; Soniprep 150; Sanyo). The clarified lysate obtained after centrifugation at 10,000 × *g* for 10 min at 4°C was injected on a HisTrap Talon crude 1-mL (Cytiva) affinity column. The selected fractions obtained upon elution using a 5 to 500 mM imidazole gradient were concentrated using an Amicon Ultra filter (10-kDa cutoff), 4°C, 4,000 × *g*. The imidazole was removed by several washings using an Amicon Ultra filter. To obtain as much isolated protein as possible, the fraction of unbound proteins was subjected to the same isolation protocol.

For all purified BVMOs, total protein concentration was determined using a DS-11 spectrophotometer (DeNovix) or a BCA protein assay kit (Sigma-Aldrich). Proteins were separated on a 4 to 20% stain-

free precast SDS-PAGE gel (Mini-Protein TGX; Bio-Rad) revealed by tryptophan fluorescence enhanced when exposed to UV light (GelDoc, stain-free imaging technology; Bio-Rad) and stained with InstantBlue (Expedeon). Quantification of protein bands on the gel was estimated by densitometry analysis using ImageLab (Bio-Rad).

Immunoblotting. Total cell lysates and eluted proteins were fractionated on a 4 to 20% stain-free precast SDS-PAGE gel (Mini-Protein TGX; Bio-Rad) and then transferred to a 0.4- μ m nitrocellulose membrane using the Transblot Turbo semidry transfer method (Bio-Rad). Following the transfer, 6 \times His-tagged BVMOs were detected using mouse monoclonal anti-poly(His) antibodies (Sigma-Aldrich) diluted 1/5,000; horseradish peroxidase (HRP)-conjugated goat antibodies against mouse (Bio-Rad), diluted 1/5,000, were used as secondary antibodies. Detections were performed with the Amersham 383 ECL Prime Western blotting reagent kit (GE Healthcare). Immunoreactive bands were revealed and measured with the ChemiDoc imaging system (Bio-Rad).

BVMO activity assay. The assays were performed at 25°C with the UV mc^2 spectrophotometer (SAFAS Monaco) in quartz cuvettes in a 450- μ L reaction mixture (50 mM HEPES, pH 7.5, bovine serum albumin [BSA; 2 μ M], NADPH [200 μ M]). The activity was measured by monitoring the oxidation of NADPH at 340 nm ($\epsilon_{340} = 6,220 \text{ M}^{-1} \cdot \text{cm}^{-1}$) for 2 to 4 min. Cyclohexanone (CH, CAS no. 3249-68-1), 2-octanone (2-oct, CAS no. 111-13-7), ethyl 3-oxohexanoate (Et3-ox, CAS no. 3249-68-1), and thioanisole (ThioA, CAS no. 100-68-5) were provided by Sigma-Aldrich, prepared in ethanol at 60 mM, and used at 5 mM in the assay, except for thioanisole, which was prepared at 12 mM and used at 1 mM. Rv0565c, Rv0892, MymA, and EthA produced in *M. smegmatis* and purified as described above were used at 10 to 40 μ g/mL. CHMO commercial enzyme was provided by Sigma-Aldrich and used at 0.05 U. Calculated activities represent nanomoles of NADPH consumed per minute per milligram of enzyme. Each experiment was performed at least in biological duplicates (independent cultures and protein purification batches) and at least in technical triplicates.

Steady-state kinetics of MymA. Kinetic parameters were determined using 96-well microplates (Nunc 96) in a CLARIOstar^{plus} (BMG Labtech) plate reader. The reaction mixture (in a 250- μ L final volume) contained 50 mM HEPES, pH 7.5, NaCl (50 mM), NADPH (500 μ M), BSA (2 μ M), 0 to 5 mM substrate, and purified MymA produced in *E. coli* at 20 μ g/mL. Reactions were started by addition of enzyme and followed during 9 min (30 cycles, 22 flashes per well and cycle) at 340 nm and 25°C to follow consumption of NADPH.

Statistical analysis. Statistical analysis was carried out and subsequent figures were made under an R (v4.0.3) working environment and with RStudio interface (v1.2.5001) (35, 36). Base stats packages were used for standard procedures such as linear regression or ANOVA. Four-parameter log-logistic dose-response models were built and treated with the drc (v3.0.1) (37). Benjamini-Hochberg (BH) *P* value correction was duly implemented using the multcomp (v1.4.16) package (38, 39). The same package was used to produce general linear hypothesis *post hoc* tests. Data wrangling and visualization of results were handled with Tidyverse (v1.3.0) (40). R source codes are available upon request.

SUPPLEMENTAL MATERIAL

Supplemental material is available online only.

FIG S1, TIF file, 0.2 MB.

FIG S2, TIF file, 0.4 MB.

FIG S3, TIF file, 0.04 MB.

FIG S4, TIF file, 0.1 MB.

FIG S5, TIF file, 0.1 MB.

TABLE S1, DOCX file, 0.01 MB.

TABLE S2, DOCX file, 0.01 MB.

ACKNOWLEDGMENTS

We acknowledge Samantha Samson (INRAE) and Marco Bellinzoni (Institut Pasteur) for fruitful discussion and Patricia Constant (IPBS) for contribution in methodology. We also thank Laure Souillès, Aurore Pérault, and Adrien Delpal for their technical help in the early phase of the project.

We are grateful to the Ministry of Higher Education, Research and Innovation for fellowships to N.T., D.L., and M.C. and to the Slovak Research and Development Agency (grant no. APVV-19-0189).

Author contributions were as follows: conceptualization, A.L., G.A., and H.M.; methodology, N.T., D.L., M.C., N.-H.L., A.P., S.M., V.M., and N.E.; validation, N.E. and M.D.; formal analysis, N.T., D.L., S.M., V.M., D.R., J.K., and N.E.; investigation, A.L., G.A., H.M., and M.D.; data curation, N.T., D.L., D.R., and A.L.; visualization, N.T., D.L., M.C., S.M., and D.R.; supervision, A.L., G.A., V.G., J.K., H.M., and M.D.; writing—original draft preparation, N.T., D.L., D.R., A.L., G.A., and H.M.; writing—review and

editing, A.L., G.A., V.G., L.M., J.K., and H.M. All authors have read and agreed to the published version of the manuscript.

The authors declare no conflict of interest.

REFERENCES

- World Health Organization. 2021. World health statistics 2021: monitoring health for the SDGs, sustainable development goals. World Health Organization, Geneva, Switzerland. <https://apps.who.int/iris/handle/10665/342703>.
- DeBarber AE, Mdluli K, Bosman M, Bekker LG, Barry CE. 2000. Ethionamide activation and sensitivity in multidrug-resistant *Mycobacterium tuberculosis*. *Proc Natl Acad Sci U S A* 97:9677–9682. <https://doi.org/10.1073/pnas.97.17.9677>.
- Moure AL, Narula G, Sorrentino F, Bojang A, Tsui CKM, Sao Emami C, Porras-De Francisco E, Díaz B, Rebollo-López MJ, Torres-Gómez PA, López-Román EM, Camino I, Casado Castro P, Guíjarro López L, Ortega F, Ballell L, Barros-Aguirre D, Remuñán Blanco M, Av-Gay Y. 2020. MymA bioactivated thioalkylbenzoxazole prodrug family active against *Mycobacterium tuberculosis*. *J Med Chem* 63:4732–4748. <https://doi.org/10.1021/acs.jmedchem.0c00003>.
- Baulard AR, Betts JC, Engohang-Ndong J, Quan S, McAdam RA, Brennan PJ, Locht C, Besra GS. 2000. Activation of the pro-drug ethionamide is regulated in mycobacteria. *J Biol Chem* 275:28326–28331. <https://doi.org/10.1074/jbc.M003744200>.
- Grant SS, Wellington S, Kawate T, Desjardins CA, Silvis MR, Wivagg C, Thompson M, Gordon K, Kazyanskaya E, Nietupski R, Haseley N, Iwase N, Earl AM, Fitzgerald M, Hung DT. 2016. Baeyer-Villiger monooxygenases EthA and MymA are required for activation of replicating and non-replicating *Mycobacterium tuberculosis* inhibitors. *Cell Chem Biol* 23:666–677. <https://doi.org/10.1016/j.chembiol.2016.05.011>.
- Hicks ND, Carey AF, Yang J, Zhao Y, Fortune SM. 2019. Bacterial genome-wide association identifies novel factors that contribute to ethionamide and prothionamide susceptibility in *Mycobacterium tuberculosis*. *mBio* 10: e00616-19. <https://doi.org/10.1128/mBio.00616-19>.
- Tolmie C, Smit MS, Opperman DJ. 2019. Native roles of Baeyer-Villiger monooxygenases in the microbial metabolism of natural compounds. *Nat Prod Rep* 36:326–353. <https://doi.org/10.1039/c8np00054a>.
- Singh A, Jain S, Gupta S, Das T, Tyagi AK. 2003. mymA operon of *Mycobacterium tuberculosis*: its regulation and importance in the cell envelope. *FEMS Microbiol Lett* 227:53–63. [https://doi.org/10.1016/S0378-1097\(03\)00648-7](https://doi.org/10.1016/S0378-1097(03)00648-7).
- Singh A, Gupta R, Vishwakarma RA, Narayanan PR, Paramasivan CN, Ramanathan VD, Tyagi AK. 2005. Requirement of the mymA operon for appropriate cell wall ultrastructure and persistence of *Mycobacterium tuberculosis* in the spleens of guinea pigs. *J Bacteriol* 187:4173–4186. <https://doi.org/10.1128/JB.187.12.4173-4186.2005>.
- Ang MLT, Zainul Rahim SZ, Siti ZZR, Shui G, Dianiškova P, Madacki J, Lin W, Koh VHQ, Martínez Gomez JM, Sudarkodi S, Bendt A, Wenk M, Mikušová K, Korduláková J, Pethe K, Alonso S. 2014. An *ethA-ethR*-deficient *Mycobacterium bovis* BCG mutant displays increased adherence to mammalian cells and greater persistence in vivo, which correlate with altered mycolic acid composition. *Infect Immun* 82:1850–1859. <https://doi.org/10.1128/IAI.01332-13>.
- Fürst MJL, Romero E, Gómez Castellanos JR, Fraaije MW, Mattevi A. 2018. Side-chain pruning has limited impact on substrate preference in a promiscuous enzyme. *ACS Catal* 8:11648–11656. <https://doi.org/10.1021/acscatal.8b03793>.
- Lennon BW, Williams CH, Ludwig ML. 2000. Twists in catalysis: alternating conformations of *Escherichia coli* thioredoxin reductase. *Science* 289: 1190–1194. <https://doi.org/10.1126/science.289.5482.1190>.
- Malito E, Alfieri A, Fraaije MW, Mattevi A. 2004. Crystal structure of a Baeyer-Villiger monooxygenase. *Proc Natl Acad Sci U S A* 101:13157–13162. <https://doi.org/10.1073/pnas.0404538101>.
- Mori G, Chiarelli LR, Esposito M, Makarov V, Bellinzoni M, Hartkoorn RC, Degiacomi G, Boldrin F, Ekins S, de Jesus Lopes Ribeiro AL, Marino LB, Centárová I, Svetlíková Z, Blaško J, Kazakova E, Lepioshkin A, Barilone N, Zanon G, Porta A, Fondi M, Fani R, Baulard AR, Mikušová K, Alzari PM, Manganelli R, de Carvalho LPS, Riccardi G, Cole ST, Pasca MR. 2015. Thio-phenecarboxamide derivatives activated by EthA kill *Mycobacterium tuberculosis* by inhibiting the CTP synthetase PyrG. *Chem Biol* 22:917–927. <https://doi.org/10.1016/j.chembiol.2015.05.016>.
- Farjallah A, Chiarelli LR, Forbak M, Degiacomi G, Danel M, Goncalves F, Carayon C, Seguin C, Fumagalli M, Záhorská M, Vega E, Abid S, Grzegorzewicz A, Jackson M, Peixoto A, Korduláková J, Pasca MR, Lherbet C, Chassaing S. 2021. A coumarin-based analogue of thiacetazone as dual covalent inhibitor and potential fluorescent label of HadA in *Mycobacterium tuberculosis*. *ACS Infect Dis* 7:552–565. <https://doi.org/10.1021/acsinfecdis.0c00325>.
- Bonsor D, Butz SF, Solomons J, Grant S, Fairlamb IJS, Fogg MJ, Grogan G. 2006. Ligation independent cloning (LIC) as a rapid route to families of recombinant biocatalysts from sequenced prokaryotic genomes. *Org Biomol Chem* 44:1252–1260. <https://doi.org/10.1039/b517338h>.
- Le N-H, Molle V, Eynard N, Miras M, Stella A, Bardou F, Galandrin S, Guillet V, André-Leroux G, Bellinzoni M, Alzari P, Mourey L, Burlet-Schiltz O, Daffé M, Marrakchi H. 2016. Ser/Thr phosphorylation regulates the fatty acyl-AMP ligase activity of FadD32, an essential enzyme in mycolic acid biosynthesis. *J Biol Chem* 291:22793–22805. <https://doi.org/10.1074/jbc.M116.748053>.
- Fraaije MW, Kamerbeek NM, Heidekamp AJ, Fortin R, Janssen DB. 2004. The prodrug activator EtaA from *Mycobacterium tuberculosis* is a Baeyer-Villiger monooxygenase. *J Biol Chem* 279:3354–3360. <https://doi.org/10.1074/jbc.M307770200>.
- Fraaije MW, Kamerbeek NM, van Berkel WJH, Janssen DB. 2002. Identification of a Baeyer-Villiger monooxygenase sequence motif. *FEBS Lett* 518: 43–47. [https://doi.org/10.1016/S0014-5793\(02\)02623-6](https://doi.org/10.1016/S0014-5793(02)02623-6).
- Korduláková J, Janin YL, Liav A, Barilone N, Dos Vultos T, Rauzier J, Brennan PJ, Gicquel B, Jackson M. 2007. Isoxyl activation is required for bacteriostatic activity against *Mycobacterium tuberculosis*. *Antimicrob Agents Chemother* 51:3824–3829. <https://doi.org/10.1128/AAC.00433-07>.
- Grzegorzewicz AE, Eynard N, Quémard A, North EJ, Margolis A, Lindenberger JJ, Jones V, Korduláková J, Brennan PJ, Lee RE, Ronning DR, McNeil MR, Jackson M. 2015. Covalent modification of the *Mycobacterium tuberculosis* FAS-II dehydratase by isoxyl and thiacetazone. *ACS Infect Dis* 1:91–97. <https://doi.org/10.1021/id500032q>.
- Romero E, Castellanos JRG, Mattevi A, Fraaije MW. 2016. Characterization and crystal structure of a robust cyclohexanone monooxygenase. *Angew Chem Int Ed Engl* 55:15852–15855. <https://doi.org/10.1002/anie.201608951>.
- Mascotti ML, Lapadula WJ, Juri Ayub M. 2015. The origin and evolution of Baeyer-Villiger monooxygenases (BVMOs): an ancestral family of flavin monooxygenases. *PLoS One* 10:e0132689. <https://doi.org/10.1371/journal.pone.0132689>.
- Rice P, Longden I, Bleasby A. 2000. EMBOSS: the European Molecular Biology Open Software Suite. *Trends Genet* 16:276–277. [https://doi.org/10.1016/S0168-9525\(00\)00204-2](https://doi.org/10.1016/S0168-9525(00)00204-2).
- Lemoine F, Correia D, Lefort V, Doppelt-Azeroual O, Mareuil F, Cohen-Boulakia S, Gascuel O. 2019. NGPhylogeny.fr: new generation phylogenetic services for non-specialists. *Nucleic Acids Res* 47:W260–W265. <https://doi.org/10.1093/nar/gkz303>.
- Letunic I, Yamada T, Kanehisa M, Bork P. 2008. iPath: interactive exploration of biochemical pathways and networks. *Trends Biochem Sci* 33: 101–103. <https://doi.org/10.1016/j.tibs.2008.01.001>.
- Söding J, Biegert A, Lupas AN. 2005. The HHpred interactive server for protein homology detection and structure prediction. *Nucleic Acids Res* 33:W244–W248. <https://doi.org/10.1093/nar/gki408>.
- Sali A, Blundell TL. 1993. Comparative protein modelling by satisfaction of spatial restraints. *J Mol Biol* 234:779–815. <https://doi.org/10.1006/jmbi.1993.1626>.
- Thompson JD, Higgins DG, Gibson TJ. 1994. CLUSTAL W: improving the sensitivity of progressive multiple sequence alignment through sequence weighting, position-specific gap penalties and weight matrix choice. *Nucleic Acids Res* 22:4673–4680. <https://doi.org/10.1093/nar/22.22.4673>.
- Robert X, Gouet P. 2014. Deciphering key features in protein structures with the new ENDscript server. *Nucleic Acids Res* 42:W320–W324. <https://doi.org/10.1093/nar/gku316>.
- Chen VB, Arendall WB, Headd JJ, Keedy DA, Immormino RM, Kapral GJ, Murray LW, Richardson JS, Richardson DC. 2010. MolProbity: all-atom structure validation for macromolecular crystallography. *Acta Crystallogr D Biol Crystallogr* 66:12–21. <https://doi.org/10.1107/S0907444909042073>.

32. Lindahl E, Hess B, van der Spoel D. 2001. GROMACS 3.0: a package for molecular simulation and trajectory analysis. *J Mol Model* 7:306–317. <https://doi.org/10.1007/s008940100045>.
33. Morris GM, Huey R, Lindstrom W, Sanner MF, Belew RK, Goodsell DS, Olson AJ. 2009. AutoDock4 and AutoDockTools4: automated docking with selective receptor flexibility. *J Comput Chem* 30:2785–2791. <https://doi.org/10.1002/jcc.21256>.
34. Dhiman RK, Schulbach MC, Mahapatra S, Baulard AR, Vissa V, Brennan PJ, Crick DC. 2004. Identification of a novel class of ω ,E,E-farnesyl diphosphate synthase from *Mycobacterium tuberculosis*. *J Lipid Res* 45:1140–1147. <https://doi.org/10.1194/jlr.M400047-JLR200>.
35. RStudio. 2021. Open source & professional software for data science teams. <https://rstudio.com/>. Retrieved 27 May 2021.
36. R Core Team. 2020. European Environment Agency. Methodology reference. <https://www.eea.europa.eu/data-and-maps/indicators/oxygen-consuming-substances-in-rivers/r-development-core-team-2006>. Retrieved 27 May 2021.
37. Ritz C, Baty F, Streibig JC, Gerhard D. 2015. Dose-response analysis using R. *PLoS One* 10:e0146021. <https://doi.org/10.1371/journal.pone.0146021>.
38. Hothorn T, Bretz F, Westfall P. 2008. Simultaneous inference in general parametric models. *Biom J* 50:346–363. <https://doi.org/10.1002/bimj.200810425>.
39. Benjamini Y, Hochberg Y. 1995. Controlling the false discovery rate: a practical and powerful approach to multiple testing. *J R Stat Soc Series B Stat Methodol* 57:289–300. <https://doi.org/10.1111/j.2517-6161.1995.tb02031.x>.
40. Wickham H, Averick M, Bryan J, Chang W, McGowan LD, François R, Grolemund G, Hayes A, Henry L, Hester J, Kuhn M, Pedersen TL, Miller E, Bache SM, Müller K, Ooms J, Robinson D, Seidel DP, Spinu V, Takahashi K, Vaughan D, Wilke C, Woo K, Yutani H. 2019. Welcome to the Tidyverse. *Journal Open Source Softw* 4:1686. <https://doi.org/10.21105/joss.01686>.